**Z. A. Mikhaylovskaya[1], M. V. Morozova[1],
E. S. Buyanova[1], S. A. Petrova[2],
I. V. Nikolaenko[3], D. G. Kellerman[3]**

[1] *Ural Federal University, 19 Mira St.,
Ekaterinburg, 620000, Russia*
[2] *Institute of Metallurgy UB RAS, 101 Amundsen St.,
Ekaterinburg, 620016, Russia*
[3] *Institute of Solid State Chemistry UB RAS,
91 Pervomayskaya St., Ekaterinburg, 620990, Russia*

Preparation and characterization of $Bi_{26-2x}Mn_{2x}Mo_{10}O_{69-d}$ and $Bi_{26.4}Mn_{0.6}Mo_{10-2y}Me_{2y}O_{69-d}$ (Me = V, Fe) solid solutions

Single phase samples of bismuth molybdate, $Bi_{26}Mo_{10}O_{69}$, doped with Mn on the bismuth sublattice and V, Fe on the molybdenum sublattice were found to crystallize in the triclinic $Bi_{26}Mo_{10}O_{69}$ structure at low doping levels and in the monoclinic $Bi_{26}Mo_{10}O_{69}$ structure – at higher dopant concentration. The assumption that Mn ions have an oxidation state of +2 was confirmed by means of magnetic measurement results analysis using Curie–Weiss law. Conductivity was investigated using impedance spectroscopy. The conductivity of $Bi_{26.4}Mn_{0.6}Mo_{9.6}Fe_{0.4}O_{69-d}$ was $1.2 \cdot 10^{-2}$ S·cm^{-1} at 973 K and $2.2 \cdot 10^{-4}$ S·cm^{-1} at 623 K, and the conductivity of $Bi_{26.4}Mn_{0.6}Mo_{9.2}V_{0.8}O_{69-d}$ was $2.2 \cdot 10^{-3}$ S·cm^{-1} at 973 K and $2.2 \cdot 10^{-5}$ S·cm^{-1} at 623 K, respectively.

Keywords: bismuth molybdates, solid electrolyte, columnar structure

Introduction

Bi_2O_3-based complex oxides exhibit a variety of properties including high oxide-ion conductivity and/or electronic conductivity at medium temperatures (573–973 K), ferroelectric and magnetic effects, as well as catalytic activity. These compounds crystallize in a number of different structure types, for example fluorite-type structures (δ-Bi_2O_3-based complex oxides [1]), layered Aurivillius type structures (the BIMEVOX family [2]) or unique columnar structures ($Bi_{26}Mo_{10}O_{69}$ [3]). The latter is reported to contain $[Bi_{12}O_{14}]_\infty$ columns oriented along the *y*-axis, MoO_n polyhedrons and «isolated» Bi^{3+} ions [4]. $Bi_{26}Mo_{10}O_{69}$ exhibits pure one-dimensional oxide ion transport along the columnar fragments (*y* axis) [5]. The values of ionic conductivity are close to that observed in the BIMEVOX and stabilized zirconia oxide ion conductors [6]. Hence $Bi_{26}Mo_{10}O_{69}$-based materials are being considered as alternative electrolytic materials for gas conversion

membranes, separators, sensors and fuel cells.

$Bi_{26}Mo_{10}O_{69}$ is part of a small solid solution range in the Bi_2O_3-MoO_3 system ($2.57 \leq Bi/Mo \leq 2.77$) [5]. A reversible monoclinic to triclinic phase transition is observed on cooling at *c.a.* 310 °C, resulting in a significant decrease in ionic conductivity and an increase in activation energy. The structure of the monoclinic form was described in [5] with the following unit cell parameters: $a = 11.74$ Å, $b = 5.80$ Å, $c = 24.79$ Å, $\beta = 102.84°$ with $P2/c$ space group symmetry. The monoclinic model includes bismuthate columns, «isolated» Bi^{3+} ions and MoO_4 tetrahedra. However, the model only accounted for 68 of the 69 oxygen atoms per formula unit required to maintain electroneutrality. The structure of the triclinic form with one additional oxygen position was suggested in [7]. It includes MoO_5 polyhedra as well as MoO_4 tetrahedra.

Solid solution formation in the $Bi_{26}Mo_{10}O_{69}$ system can be realized by substitution of either Bi^{3+} or Mo^{6+} cations. $Bi_{26}Mo_{10-2y}Me_{2y}O_{69-\delta}$ solid solutions have been reported for Me = Li, Mg, Al, Si, Ge [8]; Co [9]; V, P, W [6], while, larger cations can be substituted for bismuth including Pb [10]; Ln [11]; Ca, Sr, Ba [6] and Mn [12]. It was shown previously that the best conductivity properties of $Bi_{26-2x}Mn_{2x}Mo_{10}O_{69-d}$ series was related to the $x = 0.3$ compound [12]. The present work is devoted to the following investigation of $Bi_{26-2x}Mn_{2x}Mo_{10}O_{69-d}$ series and the synthesis, and electrical characterization of new substituted bismuth molybdates $Bi_{26-2x}Mn_{2x}Mo_{10-2y}V_{2y}O_{69-d}$ and $Bi_{26-2x}Mn_{2x}Mo_{10-2y}Fe_{2y}O_{69-d.}$

Experimental

Polycrystalline samples of general formula $Bi_{26-2x}Mn_{2x}Mo_{10}O_{69-d}$ and $Bi_{26-2x}Mn_{2x}Mo_{10-2y}Me_{2y}O_{69-d}$ were prepared using Bi_2O_3 (99.9 %), MoO_3 (99.5 %), MnO (99.7 %), V_2O_5 (99.5 %) Fe_2O_3 (99.5 %) as precursors. In each case, stoichiometric mixtures of the starting materials were thoroughly ground in an agate mortar with ethanol as a dispersant. After drying in air, pellets were pressed and placed on a bed of unreacted powder in an alumina crucible. The pellets were heated to 823 K for 48 h, followed by quenching, regrinding and re-pelletizing. The samples were then heated at 1123 K for 24 h, followed by slow cooling in air to the room temperature.

The solubility limits (x and y) and crystal structure of $Bi_{26-2x}Mn_{2x}Mo_{10}O_{69-d}$, $Bi_{26-2x}Mn_{2x}Mo_{10-2y}V_{2y}O_{69-d}$ and $Bi_{26-2x}Mn_{2x}Mo_{10-2y}Fe_{2y}O_{69-d}$ were determined by X-ray powder diffraction (XRPD). X-ray powder diffraction data were obtained on a Bruker Advance D8 diffractometer with a VÅNTEC1 detector using the Cu-Kα radiation ($\lambda_1 = 1.54056$ Å and $\lambda_2 = 1.54439$ Å). Data were collected in flat plate θ/θ geometry and calibrated against external Si standard in the 2θ range 5–70°, in steps of 0.021356°, with an effective scan time of 1 s per step. XRPD data were obtained using the equipment of the Centre for Shared Use «Ural-M» (Institute of Metallurgy UB RAS, Ekaterinburg).

The size of the particles of the powders was studied by means of the laser diffraction method using a SALD-7101 Shimadzu analyzer. The morphology of the obtained powders and their chemical composition were studied using the JEOL JSM 6390LA with a JED 2300 EDX-analyzer. Hydrostatic weighting

(Archimedes method) was used for investigation of density of ceramic pellets covered with a thin layer of waterproof coating. The volume porosity of ceramic samples was obtained by comparing for the experimental and theoretical (X-ray) densities of the samples. The variable temperature measurements of magnetic susceptibility were collected on SQUID magnetometer MPMS XL7, Quantum Design (Ural Center for Shared Use «Modern nanotechnology», Ural Federal University, Ekaterinburg).

The impedance spectroscopy method was used for electrochemical characterization of the ceramic samples of substituted $Bi_{26}Mo_{10}O_{69}$ in the range of 523–1123 K using Elinz-3000 impedance spectrometer. For the impedance measurements the samples were pelletized at 20 bar to yield pellets of 10 mm in diameter and *ca*. 2.5 mm thickness. The pressed pellets were then heated to 1123 K for 24 h, before slow cooling in air to room temperature. Platinum electrodes were applied to the pellets by covering them with a thin layer of $NH_4(PtCl_6)$ following its decomposition at *ca*. 673 K. For the analysis of impedance plots the equivalent electrical circuits method was used (Zview software, Version 2.6b, Scribner Associates, Inc.).

Results and discussion

Characterization of ceramic and powder samples

The solid solutions limit for $Bi_{26-2x}Mn_{2x}Mo_{10}O_{69-d}$ determined by XRPD is $x = 0.8$. The solubility limits of $Bi_{26-2x}Mn_{2x}Mo_{10-2y}V_{2y}O_{69-d}$ and $Bi_{26-2x}Mn_{2x}Mo_{10-2y}Fe_{2y}O_{69-d}$ are $y = 0.4$ and $y = 0.2$, respectively. Compositions with low dopant content crystallized in the triclinic structure ($y = 0.1$), whereas the compositions with higher dopant content showed the monoclinic structure of $Bi_{26}Mo_{10}O_{69-d}$ [5]. The refined unit cell parameters of the Mn + Fe and Mn+V doped bismuth molybdates are given in Tables 1 and 2, respectively. They show general compression of unit cell with increase of y and a good adherence to Vegard's law in the ranges of monoclinic modification. Decrease of homogeneity ranges as compared with $Bi_{26}Mo_{10-2y}Fe_{2y}O_{69-d}$ ($y < 0.3$ [13]) and $Bi_{26}Mo_{10-2y}V_{2y}O_{69-d}$ ($y < 0.7$ [6]) can be ex-

Table 1

Unit Cell Parameters of $Bi_{26-2x}Mn_{2x}Mo_{10-2y}V_{2y}O_{69-d}$

y	Modification	$a\pm0.002$, Å	$b\pm0.001$, Å	$c\pm0.005$, Å	$\alpha\pm0.01$, °	$\beta\pm0.01$, °	$\gamma\pm0.01$, °	$V\pm0.01$, Å3
0.1	tricl	11.751	5.858	24.561	89.80	102.19	89.20	1652.59
0.2	monocl	11.851	5.856	24.560	90	102.19	90	1666.02
0.3	monocl	11.847	5.851	24.540	90	102.27	90	1662.18
0.4	monocl	11.847	5.845	24.535	90	102.23	90	1660.39

Table 2

Unit Cell Parameters of $Bi_{26-2x}Mn_{2x}Mo_{10-2y}Fe_{2y}O_{69-d}$

y	Modification	$a\pm0.002$, Å	$b\pm0.001$, Å	$c\pm0.005$, Å	$\alpha\pm0.01$, °	$\beta\pm0.01$, °	$\gamma\pm0.01$, °	$V\pm0.01$, Å³
0.1	monocl	11.731	5.796	24.772	90	102.82	90	1642.333
0.2	monocl	11.728	5.795	24.764	90	102.74	90	1641.619

plained by the distortion of MoO_n polyhedra, caused by Mn presence.

In the present work, as well as in [12], Mn ions were assumed to have an oxidation state of +2. The measurements of magnetic susceptibility vs. temperature gave a good adherence to Curie–Weiss law (Fig. 1). The calculated parameters of Curie–Weiss law are given in the Table 3. Calculated magnetic moment for Mn is 5.95 while the theoretical value assuming Mn^{+2} is 5.92. Thus manganese is a bivalent dopant, which is typical for bismuth sublattice.

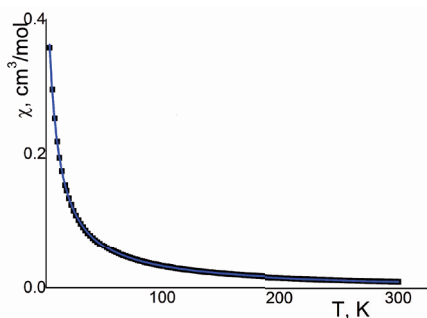Fig. 1. The magnetic susceptibility of $Bi_{24.4}Mn_{1.6}Mo_{10}O_{69-d}$ sample vs temperature. Points are experimental data, solid line – model curve (Curie–Weiss law)

Representative electron micrographs of powdered and ceramic samples are shown in Fig. 2. SEM micrographs of powdered samples showed a homogenous distribution of large and small grains (Fig. 2 a to d), with grain sizes in the range ~0.1–10 μm for all samples, which correlates well with the results of laser dispersion analysis. After sintering of pellets, dense ceramic samples were formed (Fig. 2 a to c). The majority of pores is isolated and has a spherical form. Sintered ceramic pellets' densities of more than 97 % of the theoretical (X-ray) density were confirmed by the Archimedes method. The EDX analysis showed that the concentration of dopants was close to theoretical, whereas concentrations of bismuth and molybdenum couldn't be determined separately because of the overlapping of analytical peaks. The concentration of all dopants confirms the theoretical formula within the experimental errors.

Electrical conductivity

Impedance spectroscopy was used for the electrochemical characterization of the ceramic samples. Fig. 3 (a, b) shows examples of complex plane plots of $Bi_{26.4}Mn_{0.6}Mo_{9.6}V_{0.4}O_{69-d}$ at different temperatures. This shape of complex plane plots is typical for all studied compositions. Equivalent electrical circuits for every temperature gave good agreement between calculated and experimental impedance curves. It can be seen that the shape of the complex plane plots appears to be different in different temperature regions. In general, two types of complex plane plots can be distinguished: at relatively high temperatures and at relatively low temperatures.

At high temperatures (higher than *a.c.* 823–873 K) the impedance plots of all investigated complex oxides correspond to a broadened semicircle or two separate semicircles (Fig. 3a), the high frequency intercept is non zero. The equivalent electrical circuit used for the high temperature

Table 3

Values for Curie–Weiss law $\chi = A_o + C/(T-\theta)$ and μ for $Bi_{24.4}Mn_{1.6}Mo_{10}O_{69-d}$ sample

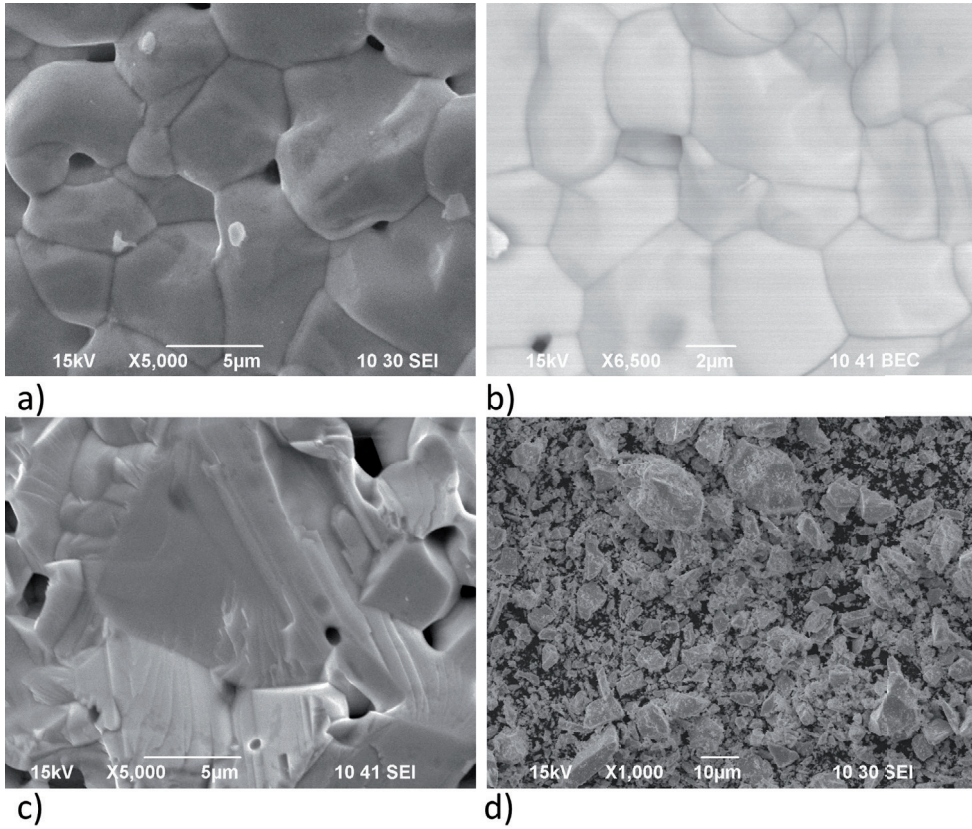| A_o cm³/mol	C, cm³*K/mol	θ, K	μ_{calc}	$\mu(Mn^{+2})_{teor}$
−0.00187	3.55	−4.7685	5.95	5.92

Fig. 2. SEM-images of $Bi_{25.4}Mn_{0.6}Mo_{9.6}V_{0.4}O_{69-d}$: *a* – ceramic pellet surface, secondary electrons imaging, scale 1:5000; *b* – ceramic pellet surface, backscattering electrons imaging, scale 1:6500; *c* – ceramic pellet cross-section, secondary electrons imaging, scale 1:5000; *d* – powder surface, secondary electrons imaging, scale 1:1000
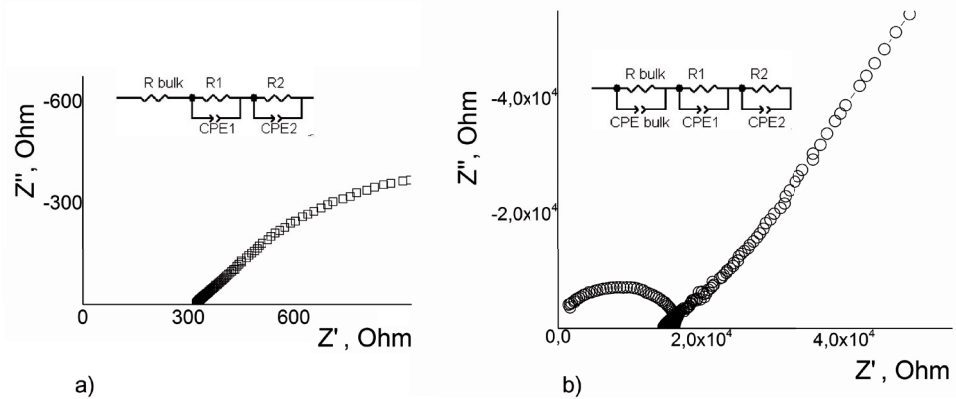

Fig. 3. Characteristic impedance plots and equivalent electrical circuits of $Bi_{26.4}Mn_{0.6}Mo_{9.2}V_{0.8}O_{69-d}$ at: *a* – high temperature region (973 K); *b* – low temperature region (623 K)

region is shown in Fig. 3a. It can be described as R1 – R2(CPE1) – R3(CPE2) serial connection, where R2 (CPE1) and R3 (CPE2) fragments are parallel connections of resistor (R) and constant phase element (CPE). The R2(CPE1) and R3(CPE2) parallel connections correspond to electrochemical processes at the electrodes (the ionic migration and interfacial processes at the electrodes), what can be confirmed by CPE1 and CPE2 capacity parameters values [14], and R1 describes bulk resistance of the sample. Grain boundary resistance wasn't observed for all compounds. The similar results were presented in [15] for $Bi_{26}Mo_{10-x}Ge_xO_{69-d}$ compounds, when only bulk resistance was observed.

At low temperatures the complex plane plots of $Bi_{26-2x}Mn_{2x}Mo_{10-2y}V_{2y}O_{69-d}$ and $Bi_{26-2x}Mn_{2x}Mo_{10-2y}Fe_{2y}O_{69-d}$ and their equivalent electrical circuits change (Fig. 3b). The impedance plot in this case consists of one separate distinct semicircle and two adjacent semi-circles. The high frequency intercept of the high-frequency semicircle is equal to zero. The equivalent electrical circuits can be described as R1(C1)–R2(CPE2)–R3(CPE3) serial connection, where R_i (CPE_i or C_i) are parallel connections of resistor (R) and constant phase element (CPE) or capacitor (C).
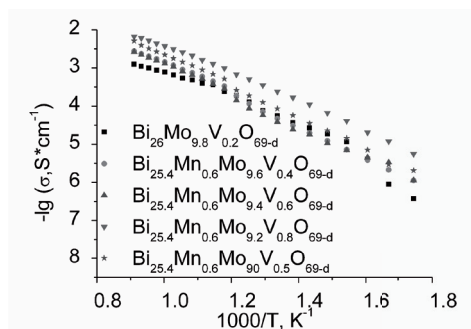
The R1(C1) connection describes the high frequency semi-circle, the C1 capacitance value is about 10^{-11} F, therefore R1 can be attributed to the total conductivity of the sample [14]. The R2(CPE2) element can be attributed to electrochemical processes at the electrodes (the «capacitance» value of CPE2 is about 10^{-6} F), R3 (CPE3) can describe complicated diffusion processes at low temperatures (the «capacitance» value of CPE2 is about 10^{-5} F).

According to the results of the impedance measurements, electrical conductivity vs. temperature dependences were plotted for $Bi_{26-2x}Mn_{2x}Mo_{10-2y}V_{2y}O_{69-d}$ and $Bi_{26-2x}Mn_{2x}Mo_{10-2y}Fe_{2y}O_{69-d}$ ceramic samples. Fig. 4 and 5 show Arrhenius plots of total conductivity of $Bi_{26-2x}Mn_{2x}Mo_{10-2y}V_{2y}O_{69-d}$ and $Bi_{26-2x}Mn_{2x-}Mo_{10-2y}Fe_{2y}O_{69-d}$. The characteristic Arrhenius plots (log (σ)–1000/T) have linear shape, and activation energy values (0.7–0.8 eV) are typical for the oxygen-ion conductors. For the parent compound $Bi_{26}Mo_{20}O_{69-d}$, a significant drop in conductivity and increase in activation energy (from 0.5–0.65 eV to 0.9 eV) is seen at temperatures below ca. 623 K due to the monoclinic to triclinic phase transition. This is not the case for the solid solutions, and it can be concluded that substitution lowers
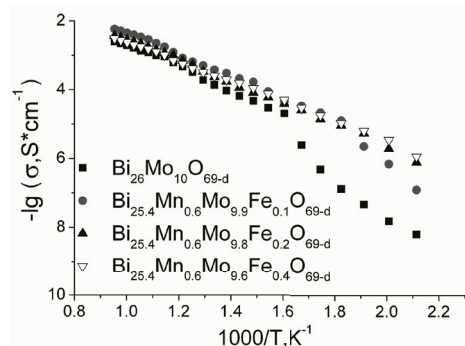

Fig. 4. Arrhenius plots of total conductivity for selected $Bi_{26-2x}Mn_{2x}Mo_{10-2y}V_{2y}O_{69-d}$ compounds

Fig. 5. Arrhenius plots of total conductivity for selected $Bi_{26-2x}Mn_{2x}Mo_{10-2y}Fe_{2y}O_{69-d}$ compounds

the monoclinic to triclinic phase transition to the temperatures below 523 K, which is the lower limit of the electrical measurements. A conductivity maximum occurs in single-phase compositions with maximum values of $y = 0.2$-0.4. The conductivity of $Bi_{26.4}Mn_{0.6}Mo_{9.6}Fe_{0.4}O_{69-d}$ was $1.2 \cdot 10^{-2}$ S·cm^{-1} at 973 K and $2.2 \cdot 10^{-4}$ S·cm^{-1} at 623 K, and the conductivity of $Bi_{26.4}Mn_{0.6}Mo_{9.2}V_{0.8}O_{69-d}$ was $2.2 \cdot 10^{-3}$ S·cm^{-1} at 973 K and $2.2 \cdot 10^{-5}$ S·cm^{-1} at 623 K, respectively. In general, the change of electroconductive properties can be explained by the increase of the electronic part of total conductivity due to the Mn doping, and by the raise of the oxygen-ion mobility due to the distortion of $Mo(Fe/V)O_n$ polyhedra.

Conclusions

The solid solutions limit for $Bi_{26-2x}Mn_{2x}Mo_{10}O_{69-d}$ is $x = 0.8$, and the solubility limits of $Bi_{26-2x}Mn_{2x}Mo_{10-2y}V_{2y}O_{69-d}$ and $Bi_{26-2x}Mn_{2x}Mo_{10-2y}Fe_{2y}O_{69-d}$ are $y = 0.4$ and $y = 0.2$, respectively. Compositions with low dopant content crystallize in the triclinic structure ($y = 0.1$), and compositions with higher dopant content – in the monoclinic structure. Mn+Fe and Mn+V doped systems were synthesized for the first time and the formation of dense ceramics of these systems has been demonstrated. In general, the change of electroconductive properties depends of dopant concentration and is influenced by the metal-oxygen polyhedra distortion and the increase of the electronic part of total conductivity.

Acknowledgements

References

1. Boivin JC. Structural and electrochemical features of oxide ion conductors. *Int J Inorg Mat.* 2001;3:1261-6. doi:10.1016/s1466-6049(01)00118-0.
2. Abraham F, Boivin JC, Mairesse G, Nowogrocki G. The bimevox series: A new family of high performances oxide ion conductors. *Solid State Ionics.* 1990;40-1:934-7. DOI:10.1016/0167-2738(90)90157-M.
3. Fonseca FC, Steil MC, Vannier RN, Mairesse G, Muccillo R. Grain-sized influence on the phase transition of $Bi_{26}Mo_9WO_{69}$: an X-ray diffraction and impedance spectroscopy study. *Solid State Ionics.* 2001;140:161-71. DOI:10.1016/S0167-2738(01)00705-6.
4. Buttrey DJ, Vogt T, Yap GPA, Rheingold AL. The structure of $Bi_{26}Mo_{10}O_{69}$. *Mater Res Bull.* 1997;32:947-62. DOI:10.1016/s0025-5408(97)00063-9.
5. Vannier RN, Mairesse G, Abraham F, Nowogorski G. $Bi_{26}Mo_{10}O_8$ solid solution type in the Bi_2O_3–MoO_3–V_2O_5 ternary diagram. *J Solid State Chem.* 1996;122:394-406. DOI:10.1006/jssc.1996.0133.
6. Vannier RN, Danze S, Nowogrocki G, Huve M, Mairesse G. A new class of mono-dimensional bismuth-based oxide anion conductors with a structure based

on $[Bi_{12}O_{14}]_{\infty}$ columns. *Solid State Ionics.* 2000;136-7:51-9. DOI:10.1016/S0167-2738(00)00351-9.

7. Ling CD, Miiller W, Johnson MR, Richard D, Rols S, Madge J, Evans IR. Local structure, dynamics, and the mechanisms of oxide ionic conduction in $Bi_{26}Mo_{10}O_{69}$. *Chem Mater.* 2012;24:4607-14. DOI:10.1021/cm303202r.

8. Bastide B, Enjalbert R, Salles P, Galy J. Ionic conductivity of the oxide family $Bi[Bi_{12}O_{14}][(Mo,M)O_4]_5$ with M=Li, Mg, Al, Si, Ge and V. *Solid State Ionics.* 2003;158:351-8. doi:10.1016/s0167-2738(02)00910-4.

9. Mikhailovskaya ZA, Buyanova ES, Petrova SA, Morozova MV, Zhukovskiy VM, Zakharov RG, Tarakina NV, Berger IF. Cobalt-doped $Bi_{26}Mo_{10}O_{69}$: crystal structure and conductivity. *J Solid State Chem.* 2013;204:9-15. DOI: 10.1016/j.jssc.2013.05.006.

10. Enjalbert R, Hasselmann G, Galy J. A new mixed oxide with $(Bi_{12}O_{14})_n$ columns: $PbBi_{12}Mo_5O_{34}$. *Acta Crystallogr, Sect C: Struct Chem.* 1997;53:269-72. DOI:10.1107/s0108270196013698.

11. Galy J, Salles P, Rozier P, Castro A. Anionic conductors $Ln_{2/3}[Bi_{12}O_{14}](MoO_4)_5$ with Ln=La, Nd, Gd, Ho, Yb. Synthesis–spark plasma sintering–structure–electric properties. *Solid State Ionics.* 2006;177:2897-902. DOI:10.1016/j.ssi.2006.07.059.

12. Mikhaylovskaya ZA, Buyanova ES, Morozova MV, Petrova SA, Nikolaenko IV. Mn-doped $Bi_{26}Mo_{10}O_{69-d}$: synthesis and characterization. *Ionics.* 2017;23:1107-14. DOI:10.1007/s11581-016-1917-5.

13. Mikhaylovskaya ZA, Morozova MV, Buyanova ES, Petrova SA Abrahams I. Iron-doped $Bi_{26}Mo_{10}O_{69}$ bismuth molybdate:synthesis, properties and structure. In: Abstract Book of the 11th international symposium on systems with fast ionic transport. 2014 Jun 25-29; Gdańsk University of Technology, Gdańsk-Sobieszewo, Poland. 2014. P. 78.

14. Irvine JTS, Sinclair DC, West AR. Electroceramics: Characterization by impedance spectroscopy. *Adv Mater.* 1990;2:132-8. DOI:10.1002/adma.19900020304.

Cite this article as (как цитировать эту статью)